Geophysical Journal International

Geophys. J. Int. (2023) **232,** 287–299
Advance Access publication 2022 August 18
GJI Seismology

https://doi.org/10.1093/gji/ggac324

Temporal changes of seismicity in Salton Sea Geothermal Field due to distant earthquakes and geothermal productions

Chenyu Li [1,2] Zhigang Peng,[1] Dongdong Yao,[3] Xiaofeng Meng[4] and Qiushi Zhai[5]

[1] *School of Earth and Atmosphere Sciences, GA Tech, 311 Ferst Dr, Atlanta, GA 30318, USA. E-mail: chenyu.li@ntu.edu.sg*
[2] *Earth Observatory of Singapore, Nanyang Technological University, 50 Nanyang Avenue, Block N2-01a-15, 639798 Singapore.*
[3] *National Key Laboratory of Geological Processes and Mineral Resources, China University of Geosciences, 430074 Wuhan, China.*
[4] *Southern CA Earthquake Center, University of Southern California, 3651 Trousdale Parkway, Suite 169, Los Angeles, California.*
[5] *Seismological Laboratory, California Institute of Technology, 1200 E. California Blvd. MS 252-21, Pasadena, CA*

Accepted 2022 August 11. Received 2022 August 9; in original form 2022 May 18

SUMMARY

The Salton Sea Geothermal Field (SSGF) is one of the most seismically active and geothermally productive fields in California. Here we present a detailed analysis of short-term seismicity change in SSGF from 2008 to 2013 during and right following large distant earthquakes, as well as long-term seismicity change due to geothermal productions. We first apply a GPU-based waveform matched-filter technique (WMFT) to the continuous data recorded by the Calenergy Borehole (EN) Network and detect more than 70 000 new micro-earthquakes than listed in the standard Southern California Seismic Network catalogue. We then analyse the seismicity rate changes in the SSGF associated with transient stress fluctuations triggered by regional and large teleseismic earthquakes from 1999 to 2019. We find triggered seismicity in the SSGF following seven regional $M > 5.5$ earthquakes. In comparison, most teleseismic earthquakes with $M > 8.0$ did not trigger significant seismicity rate change in the SSGF, likely indicating a frequency dependence in remote dynamic triggering. We further characterize the correlation between the long-term seismicity rate and geothermal production rates, and the temporal and spatial distribution of Guttenberg–Richter *b*-values inside and outside the SSGF with the newly detected catalogue. The long-term seismicity shows that events with $M > 1.5$ are likely correlated with net production rates, while smaller events do not show any correlation. The *b*-values inside the SSGF are higher than those outside the SSGF, and the locations of dynamically triggered events are close to locations with high *b*-values.

Key words: Induced seismicity; Salton Sea Geothermal field; Earthquake dynamic triggering; Waveform matched-filter technique.

1 INTRODUCTION

Geothermal energy is considered as a promising renewable energy source to reduce the greenhouse warming effects from burning fossil fuels (Panwar *et al.* 2011). However, geothermal productions such as steam/fluid removal and fluid injection are capable of altering the subsurface stress state and inducing earthquakes (Cardiff *et al.* 2018; Martínez-Garzón *et al.* 2020; Im & Avouac 2021). Although most geothermally induced seismicity are small-magnitude earthquakes, moderate-size earthquakes related to geothermal productions were also reported. These include the 2017 M_w 5.4 Pohang earthquake in South Korea and the 2006 M_L 3.4 Basel earthquake in Switzerland, raising concerns of increasing earthquake hazard by geothermal productions (Mignan et al 2015; Kim *et al.* 2018; Ellsworth *et al.* 2019; Buijze *et al.* 2020).

The Salton Sea Geothermal Field (SSGF) is located in the southern shorelines of Salton Sea in Southern California, which is a shallow saline lake within the trans-extensional Salton Trough. It is bounded by the Southern San Andreas Fault to the NE, and the Imperial Fault and the Cerro Prieto Fault to the SW (Fig. 1). There is a clear variation in surface heat flows in this region, which is likely caused by magmatic intrusion due to the rifting process along the Salton Trough (Younker *et al.* 1982). The Salton Trough is seismically active with numerous earthquake swarms, driven by aseismic creep and fluid diffusion (Lohman & McGuire 2007; Chen & Shearer 2011).

Recent studies have shown that geothermal fields in California including the SSGF are highly sensitive to external stress perturbations such as dynamic stresses caused by passing surface waves of large distant earthquakes (Gomberg & Davis 1996; Brodsky 2006; Aiken & Peng 2014; Zhang *et al.* 2017; Alfaro-Diaz *et al.* 2020; Fan *et al.* 2021). Triggered seismicity in the SSGF has been found after several $M > 7$ earthquakes at regional distances, including the 1999 M_w 7.1 Hector Mine Earthquake and 2010 M_w 7.2

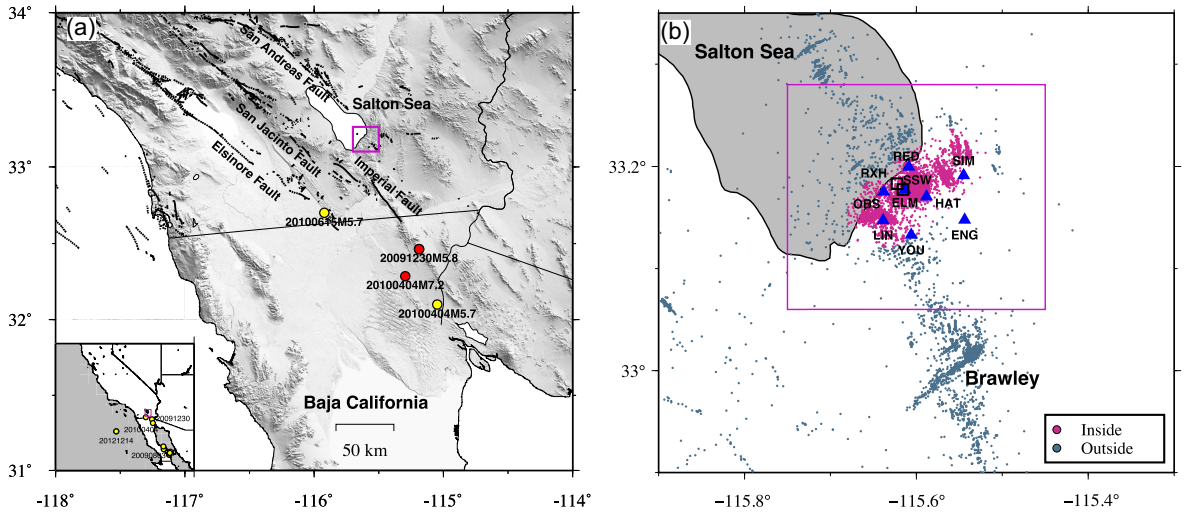

Figure 1. (a) Location of SSGF and surrounding tectonic background. The yellow circles mark selected regional target main shocks and red circles mark events with dynamic triggering in SSGF. The purple box is region in (b). (b) Template events (blue and purple dots) and EN stations (blue triangles), RXH (black square) is one broad-band station in Southern California network (network code CI) and is used for supplementary check of the waveforms. Purple dots are events within 3 km from injection/production wells, termed as inside SSGF, and blue dots are events outside SSGF. Events in the purple box are used for computing *b*-value and *Mc* in Sections 3 and 4.

El Mayor-Cucapah (EMC) Earthquake (Hough & Kanamori 2002; Meng & Peng 2014; Castro *et al.* 2017; Ross *et al.* 2019). Taira *et al.* (2018) and Zhang *et al.* (2022) also observed seismic velocity reduction in the SSGF after local and regional earthquakes, likely caused by dynamic stress transients, as well as long-term seismicity velocity increase due to poroelastic contraction during geothermal production. Brodsky & Lajoie (2013) discovered temporal correlation between background seismicity rate and net production volumn from 1982 to 2013. Spatial correlation between seismicity and injection wells has also been found in the SSGF (Chen & Shearer 2011; Cheng and Chen 2018). Detailed analysis of spatial and temporal changes of seismicity in geothermal regions can help to better understand its interaction with distant earthquakes and anthropogenic activities, and physical mechanisms of earthquake triggering and induced seismicity.

Many previous studies on seismicity changes were based on regional or global earthquake catalogues (Hill *et al.* 1993; Zhang *et al.* 2017), or manually picked earthquakes (Gomberg *et al.* 2004; Prejean *et al.* 2004; Aiken & Peng 2014). A few automatic methods have been developed to studying dynamic triggering. Alfaro-Diaz *et al.* (2020) applied a short- over long-term average ratio to automatically detect remote triggering around the Coso Geothermal Field in California. Yun *et al.* (2019, 2021) also developed a high-frequency power integral ratio algorithm to automatically detect remote triggering in the Geysers Geothermal Field in California and other region. While their methods are capable of detecting both micro-earthquakes and deep-tectonic tremors triggered by distant earthquakes, subsequent visual inspections are needed in both cases to ensure that the newly detected events are uncatalogued local earthquakes, rather than other types of high-frequency noises.

Recent studies also utilized earthquakes detected by a waveform-based matched-filter technique (WMFT) to study remote dynamic triggering (van der Elst *et al.* 2013; Wang *et al.* 2015; Yao *et al.* 2015, 2021; Johnson & Burgmann 2016; Ross *et al.* 2019; Li *et al.* 2021). The WMFT is an efficient way to detect additional seismic events in regions that are seismically active (Gibbons & Ringdal 2006; Shelly *et al.* 2007). Using events that are listed in known earthquake catalogues as templates, this technique can identify many times more events from continuous waveforms that are similar to existing templates (e.g. Peng & Zhao 2009; Ross *et al.* 2019). When compared with manual picking (e.g. Gomberg *et al.* 2004; Aiken & Peng 2014) or other forms of automatic procedures (Yun *et al.* 2019, 2021; Alfaro-Diaz *et al.* 2020), the WMFT provides more complete and consistent earthquake catalogues to examine seismicity rate change around distant main shocks. For example, Meng & Peng (2014) examined physical mechanisms of triggered seismicity in southern California by the 2010 EMC earthquake with a GPU-based WMFT (Meng *et al.* 2012). They found that dynamic stress perturbations played the most important role in triggering microseismicity at the SSGF (and other regions in Southern California) immediately following the main shock. However, the long term (i.e. a few months after the main shock) seismicity changes in SSGF and elsewhere in Southern California are mostly controlled by static stress changes from the EMC main shock. Similar conclusions are drawn by Ross *et al.* (2019), who applied the WMFT to 10-yr of continuous waveforms in Southern California. Their resulting Quake Template Matching (QTM) database (Ross *et al.* 2019) has been utilized to conduct high-resolution analysis of dynamic triggering in highly seismically active regions of Southern California (Fan *et al.* 2021; Miyazawa *et al.* 2021).

Since Meng & Peng (2014) only examined the time window one month before and four months after the 2010 EMC main shock, here we extend the GPU-based WMFT analysis to continuous seismic data recorded by the local borehole stations between 2008 and 2013, during which the continuous waveform data are openly available at the Southern California Earthquake Data Center (SCEDC). With a more complete earthquake catalogue in SSGF, we systematically analyse seismicity change after 80 $M > 5.5$ earthquakes both at local-regional distances (60–1000 km) and remote distances (>1000 km). We also manually inspect high-frequency waveforms recorded by surface seismic stations outside the study time window for additional evidence of instantaneous dynamic triggering. Finally, we compare the long-term seismicity rate with geothermal fluid injection/extraction rates, and further characterize the variation of Guttenberg–Richter *b*-values both inside and outside the

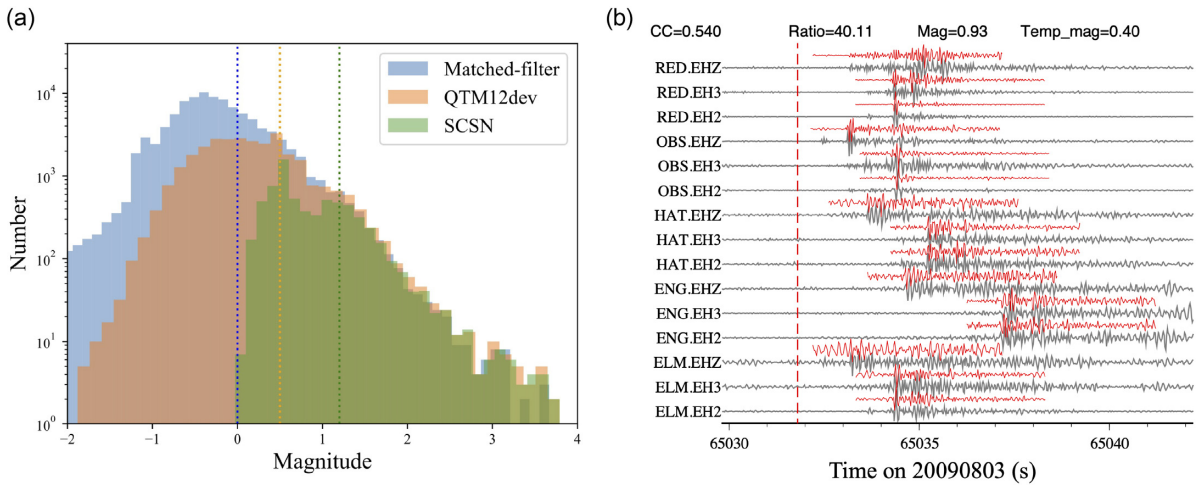

Figure 2. (a) Frequency–magnitude distribution for three catalogues. Three catalogues are: the matched filter detected (MFD) catalogue in this study, the QTM catalogue (qtm_final_12dev.hypo) from Ross *et al.* (2019), and the relocated catalogue from Hauksson *et al.* (2012) (catalogue 1981–2014), the dotted lines mark *Mc* of three catalogues. (b) Example of a detected event (origin time: 2009 August 03,18:03:51.80; magnitude: 0.93) with a CC coefficient 0.54, this event occurred 235 seconds after the 2009 August 03 M_w 6.9 Baja California Earthquake. Red and grey waveforms correspond to one template earthquake and the detected event.

geothermal field to better discern long-term evolution of seismicity patterns and its relationship with geothermal productions.

2 WAVEFORM MATCHED-FILTER DETECTION

The seismic data used in this study are from the Calenergy Borehole Network (network code: EN), which includes 8 borehole stations with continuous data open to public from 2008 to 2013 (Fig. 1). We choose the EN network because they are borehole stations and located within the SSGF, thus they provide data with high signal-to-noise ratios (SNRs) for local micro-earthquakes. The continuous recording of station EN.SIM has some data gaps, thus the continuous recording from seven stations in EN network is used for the WMFT. In addition, the waveforms from surface broad-band stations (CI.SSW and CI.RXH) are used for visual inspection of additional triggering cases. We select 8900 events from the Southern California Waveform Relocated Catalog during 2008–2013 (the updated 1981–2018 catalogue, Hauksson *et al.* 2012) as templates for detection (Fig. 1). We first bandpass filter both template and continuous waveforms between 5–20 Hz. We choose this frequency range because the borehole sensor L15B (Mark Products) has a corner frequency of 4.5 Hz. In addition, cultural and industrial noises are stronger at frequencies higher than 20 Hz. The template time window is 1 s before and 4 s after the analyst-picked *P* arrival for vertical component and *S* arrival for horizontal components. The noise window is 5 s right before the *P*-arrival time. We define SNR as the ratio between seismic energy between the *P*-wave and the noise windows. All three channels with SNRs above 3 for each station are cross-correlated with corresponding continuous waveforms by sliding one data point each time, and the cross-correlation (CC) functions of all channels are shifted back to the origin times of templates and then stacked and normalized. Detection threshold is set as the median CC value of the daily trace plus 15 times its median absolute deviation (MAD) and CC value of 0.3, whichever is higher. We use a relatively higher threshold than other recent studies (e.g. 9 or 12 times of MAD, Meng & Peng 2014; Ross *et al.* 2019), mainly because it can help to remove potential false detections contaminated by aftershocks of moderate-size earthquakes within 100 km, rather than triggered seismicity in the target regions (e.g. Meng *et al.* 2013; Meng & Peng 2014).

The magnitude of each detected event is estimated based on the magnitude of template with the highest CC value: $M_d = M_t + c * \log(R)$, where R is the median of peak amplitude ratios between the detected and template waveforms for all channels (Peng & Zhao 2009; Shelly *et al.* 2016), and a $c = 1$ for local magnitude scale. Newly detected events are assigned to the same location as the best-matching template. In this study, we do not apply further magnitude calibration or relocation methods as were done in recent studies (Shelly *et al.* 2016; Chen *et al.* 2018; Meng *et al.* 2018; Ross *et al.* 2019; Yao *et al.* 2020), mainly because the locations and magnitudes of templates in the relocated catalogue are already well constrained (Hauksson *et al.* 2012). In addition, we use a relatively higher CC threshold as compared with these studies, which ensures that the newly detected and template events are spatially closer to each other.

Fig. 2(a) shows a comparison of cumulative frequency magnitude distribution for our matched-filter detection (MFD) catalogue in this study (with a threshold of 15×MAD), the QTM catalogue (with a threshold of 12×MAD) from Ross *et al.* (2019) and the relocated catalogue of the Southern California Seismic Network (SCSN) from 2008 to 2013 (Hauksson *et al.* 2012). The total number of events is 136 016 in the MFD catalogue in a region within the rectangular grid (latitude range [33.12°, 33.22°], longitude range [−115.67°, −115.53°]), which is 3 times and 15 times of events than listed in the QTM and SCSN catalogues, respectively. Such an increase is mainly due to the fact the latter two catalogues were mostly based on waveforms/phases recorded by regional surface stations and local borehole stations, while the catalogue in this study is detected based solely on local short-period borehole recordings. The corresponding magnitude of completeness (*Mc*) as determined by the maximum curvature method (MAXC) (plus 0.4 to correct for potential bias of this method (Woessner & Wiemer 2005)) shows a clear reduction from $Mc = 1.2$ and 0.5 for the SCSN and QTM catalogues to $Mc = 0$ for the MFD catalogue obtained in this study. Fig. 2(b) shows an example of a detected event 235 s after the 2009 August 03 M_w 6.9 Baja California Earthquake. This strike-slip event appears to have unilateral super-shear rupture in the northward direction towards

the SSGF, and triggered seismicity at multiple sites in California (Fan *et al.* 2022). The magnitudes versus occurrence times of all events in the MFD and SCSN catalogues are in Fig. S1 (Supporting Information).

3 DYNAMICALLY TRIGGERED SEISMICITY

3.1 Search for dynamic triggering

To search for dynamically triggered seismicity, we first select moderate to large earthquakes ($M > 5.5$) during 2008–2013 with predicted dynamic stresses larger than 0.5 kPa at surface broad-band station RED in the SSGF. We follow the equations for computing far-field dynamic strain in van der Elst & Brodsky (2010):

$$\log_{10} A_{20} = M_s - 1.66\log_{10}\Delta - 2 \quad (1)$$

where A_{20} (μm) is the peak dynamic strain of long-period (20-s) surface waves, M_s is the surface-wave magnitudes of distant main shocks, which is set to be equal to their reported moment magnitudes M_w and Δ is the epicentral distance in degrees. Then, the dynamic strain A_{20} is converted to peak ground velocity (PGV) for the 20-s waves by the approximation PGV$\approx \frac{2\pi A_{20}}{T}$ (Aki & Richards 2002; van der Elst & Brodsky 2010). The dynamic stress change is estimated as,

$$\sigma = \frac{\mu\,(\mathrm{PGV})}{V_{ph}} \quad (2)$$

where the shear modulus is set as $\mu = 35$ GPa, and surface wave velocity $V_{ph} = 3.5\ \mathrm{km\,s^{-1}}$.

After selecting 70 target earthquakes, we compare the seismicity rate in the SSGF before their original time and after the arrival of P waves (Table S1). We compute both β-statistic value (e.g. Matthews & Reasenberg 1988; Aron & Hardebeck 2009) and Z-statistic value (Habermann 1981; Marsan & Wyss 2011), and use them as indicators of dynamic triggering. The β-statistic is defined as:

$$\beta = \frac{N_a - N(T_a/T)}{\sqrt{N(T_a/T)(1-(T_a/T))}} \quad (3)$$

where T_a is the time duration for the triggering window, while the entire window contains both the triggering and background window (T_b) before a main shock with a duration $T = T_a + T_b$, and N_a and N are numbers of earthquakes in the triggering and entire windows, respectively.

The Z-statistic value is computed as:

$$Z = \frac{N_a T_b - N_b T_a}{\sqrt{N_a T_b^2 + N_b T_a^2}} \quad (4)$$

which is a more symmetric version of the β-statistic, and is used as an additional parameter to evaluate seismicity increase (Habermann 1981; Marsan & Wyss 2011). Here, we only use the events with $M > -0.4$ for computing β- and Z-values. We note it is slightly lower than the $Mc = 0$, because some local micro-earthquakes during surface waves have $-0.4 < M < 0$. Using a smaller cut-off magnitude would include as many events as possible without biasing towards a higher positive β- and Z-values, because there are generally more missing small events immediately after the targeting distant earthquakes than before.

The β- and Z-statistic values above threshold of 2 generally indicates a significant seismicity rate increase (i.e. Hill & Prejean 2007; Marsan & Wyss 2011). Recent studies have shown that the β-statistic threshold might vary for different regions and times, especially when the N_b and T_a are too small (i.e. Prejean & Hill 2018; Pankow & Kilb 2020; Fan *et al.* 2021). The large seismicity rate fluctuations in the SSGF might also affect the judgement of dynamic triggering with β and Z thresholds of 2. Here we find an empirical threshold of β-statistic (β_E) for each main shock by randomly selecting 10 000 same time windows with T_a in the entire study period as triggering windows and compute β-statistics in the same T_b window, and set the β_E as the value that is above 95 per cent of the 10 000 β-values. The β (corresponding to triggering window during surface waves), β_E and Z for all the events are shown in Tables S3–S6 (Supporting Information), and the events with $\beta \geq \beta_E$ and $\beta > 2$ are listed in Table 1. We only perform the empirical threshold analysis for the β statistics here, because the Z-value generally changes in a similar pattern as the β-value.

3.2 Dynamic triggering from 2008 to 2013

3.2.1 Instantaneous triggering

Seismicity triggered during or immediately after surface waves of the target earthquakes are known as instantaneous dynamic triggering (e.g. Prejean *et al.* 2004; Hill and Prejean, 2007). Here we define the triggering window T_a as the arrival time window corresponding to an apparent phase velocity of 2–5 $\mathrm{km\,s^{-1}}$ plus 200 s. Because some events are less than 100 km away from the SSGF (and hence have a relatively short time window of < 33 s), we add 200 s to the triggering window to ensure that the time window is long enough for statistical significance. Both T_b of 60 and 1 d are used, to account for seismicity changes compared to both long- and short-term background seismicity.

Out of the 70 events analysed, three regional and one teleseismic earthquakes have β-values above the β_E thresholds in the triggering window: the 2009 August 03 M_w 6.9 and 2009 December 30 M_w 5.8 earthquakes in Baja California, the 2010 EMC earthquake, as well as the 2011 March 11 M_w 9.1 Tohoku-Oki, Japan earthquake (Table 1). The first three earthquakes all have β-value larger than 5, indicating statistically significant increase of seismicity following these regional events. The 2011 Tohoku-Oki main shock is more than 9000 km from the SSGF. The corresponding β-value of 4.9 equals β_E, and is smaller than other four earthquakes, so the dynamic triggering of this event is not as significant as those regional earthquakes. On the other hand, large distant earthquakes such as the 2010 February 27 M_w 8.8 Maule, Chile and the 2012 April 11 M_w 8.6 Indian Ocean earthquakes did not have corresponding β-value above the β_E threshold. Hence, they are not considered as positive dynamic triggering cases. The information of β-, β_E- and Z-values for all the events with T_b of 60 and 1 d are in Tables S3 and S4 (Supporting Information), respectively. The β- and Z-values computed with M>0 for the four earthquakes in Table 1 are shown in Table S2 (Supporting Information), indicating that the choice of smaller cut-off magnitude are not affecting the thresholds of positive dynamic triggering.

The original and high-pass-filtered waveforms of the 2009 August 03 M_w 6.9 and the 2009 December 30 M_w 5.8 earthquakes are shown in Fig. 3, with the detected events marked. Fig. S2 (Supporting Information) shows the cumulative numbers of local earthquakes in SSGF after 4 events that are listed in Table 1. The 2010 EMC and 2009 December 30 M_w 5.8 earthquakes triggered clear instantaneous increase of local seismicity, while the local seismicity

Table 1. Information of the events that have instantaneous dynamic triggering indicated by $\beta \geq \beta_E$, with T_a in surface wave window, $T_b = 60$ d.

Date	Time	Magnitude	Distance (km)	PGV (cm s^{-1})	β-value	β_E	Z-value	T_a (s)
2009/08/03	17:59:56.17	6.9	526	0.53	13.67	2.45	2.18	388.0
2009/12/30	18:48:57.33	5.8	89	1.17	7.88	−0.36	1.66	231.6
2010/04/04	22:40:42.36	7.2	103	2.06	13.24	−0.29	1.96	236.9
2011/03/11	05:46:24.12	9.1	8732	0.10	4.90	4.90	2.24	5953.5

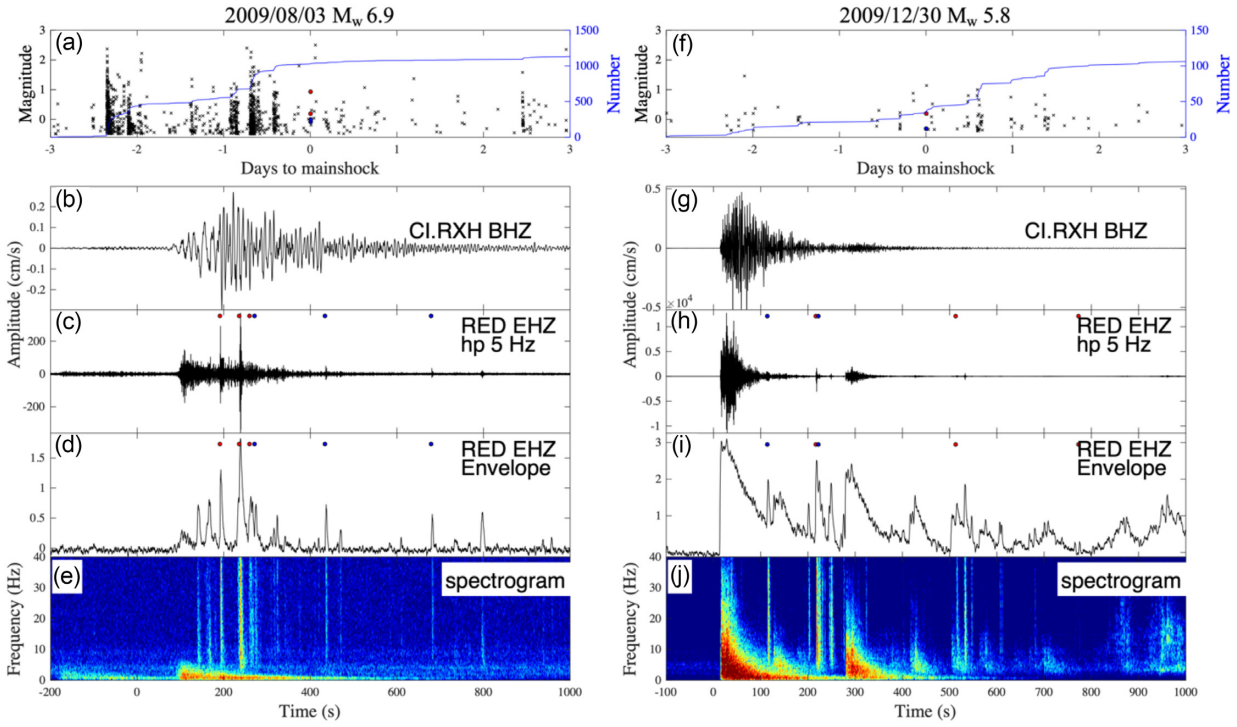

Figure 3. (a) Magnitude distribution for detected events 3 d before/after the 2009 August 03 M_w 6.9 Baja California Earthquake, (b) raw waveform recorded by the broad-band station RXH, (c) high-pass filtered (5 Hz) waveform on station RED, red circles are events with $M \geq 0$, blue circles are events with $-0.5 < M < 0$, (d) envelope of (c) and (e) spectrogram of (c). (f)–(j) Similar to (a)–(e) for the 2009 December 30 M_w 5.8 earthquake.

after 2011 March 11 M_w 9.1 earthquake showed stepwise increase with time delay of a few hours (Fig. S2, Supporting Information; Pankow & Kilb 2020).

3.2.2 Possible delayed triggering

We also compute the β-statistics with the triggering window T_a set as one day following the *P*-wave arrivals. There are three earthquakes that triggered seismicity after one day in SSGF indicated by $\beta \geq \beta_E$ (Table 2 and Tables S5 and S6, Supporting Information). Again, the 2010 EMC Earthquake triggered a clear increase of seismicity both during and after their surface waves. In contrast, the seismicity following the other three events with instantaneous dynamic triggering did not last for one day. For the 2010 January 10 M_w 6.5 and 2013 February 06 M_w 8.0 earthquakes, with increased seismicity within one day, local seismic activity started to increase after the passing of surface waves (Fig. S2, Supporting Information).

3.3 Additional evidence for dynamic triggering

To further augment our database of triggering main shocks, we examine high-frequency waveforms of additional regional $M > 5.5$ earthquakes between 1992–2007 and 2014–2020. These include the 2002 November 03 M_w 7.9 Denali Fault earthquake and a few remote $M > 8.0$ earthquakes in Sumatra and Chile, as well as several regional earthquakes (Table S6, Supporting Information). During these time periods, the waveforms of EN network are not open to public, thus we analyse any available broad-band or short-period stations around the SSGF. Before 2004, the nearest broad-band station is CI.SSW. After 2004, we analyse waveforms recorded by the broad-band station CI.RXH. In addition, the QTM catalogue (Ross *et al.* 2019) covers the time window of 2008–2017 for the entire southern California and the corresponding β-statistic value can be used as an additional indicator. For the target earthquakes before 2007 and after 2017, we search for instantaneous triggering during surface based on visual inspection of continuous data and spectrograms. For the events from 2014 to 2017, we consider the earthquakes as positive triggering if the β-value computed from QTM catalogue is above 2. We find 4 regional earthquakes that triggered seismicity in SSGF: the 1999 October 16 M_w 7.1 Hector Mine (168 km), 2003 December 22 M_w 6.5 San Simeon earthquake (576 km), the 2019 July 06 M_w 7.1 Ridgecrest earthquake (320 km) and its M_w 6.4 foreshock (Figs S4 and S5, Supporting Information). For the 2004 September 28 M_w 6.1 Parkfield and 2014 August 24 M_w 6.0 South Napa earthquake, there is no clear evidence of

Table 2. Information of the events that have dynamic triggering within 1 d indicated by $\beta \geq \beta_E$ with $T_a = 1$ d and $T_b = 60$ d.

Date	Time	Magnitude	Distance (km)	PGV (cm s^{-1})	β-value	β_E	Z-value	T_a (s)
2010/01/10	15:30:47.44	6.5	1158	0.04	5.78	5.64	4.28	86 400
2010/04/04	22:40:42.36	7.2	103	2.06	40.16	9.57	14.62	86 400
2013/02/06	01:12:27.00	8.0	9670	0.01	17.83	13.60	8.30	86 400

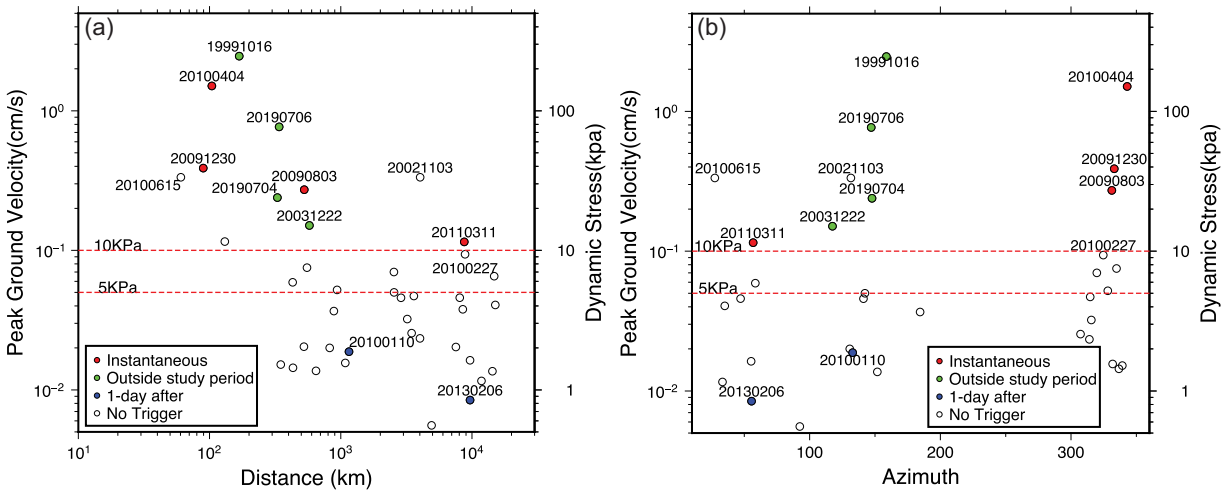

Figure 4. (a) PGV versus distance of all the earthquakes studied from 1999 to 2019 and (b) PGV and dynamic stress versus azimuth of events in this study. The corresponding estimated dynamic stress change is labelled on the right. The waveforms of events before 2004 are from station CI.SSW, and waveforms of events after 2004 are from station CI.RXH.

dynamic triggering based on the waveforms, and the β-values computed from QTM catalogue for the 2014 South Napa earthquake did not show any significant increase of seismicity, likely because the associated dynamic stress changes (both around 2 kPa) are relatively small. The 2002 November 03 M_w 7.9 Denali Fault earthquake, the 2007 September 12 M_w 8.4 Sumatra earthquake and several $M > 8$ earthquakes during 2014–2016 in Chile do not correspond to any clear change in local seismicity in the SSGF (Fig. S5 and Table S3, Supporting Information).

3.4 Threshold for dynamic triggering

Based on the aforementioned analysis, the 2009 August 03 M_w 6.9, 2009 December 30 M_w 5.8, 2010 April 04 M_w 7.2 and 2011 March 11 M_w 9.1 earthquakes have triggered seismicity in the SSGF during the passage of their surface waves. We estimate the peak dynamic stress change of all the earthquakes from the PGVs after a low-pass filter of 1 Hz (Fig. 4). All four events with instantaneous triggering (except the 2011 March 11 M_w 9.1 Tohoku-Oki earthquake) have high dynamic stress changes (>20 kPa), and they showed higher β-value above 5. For the events outside our study period (2008–2013), the 2019 July 05 M_w 7.1 Ridgecrest sequence, 2003 December 22 M_w 6.5 San Simeon and 1999 October 16 M_w 7.1 Hector Mine earthquakes also showed dynamic triggering in the SSGF. Overall, 8 out of 21 (38 per cent) regional earthquakes showed dynamic triggering in the SSGF, while only 2 out of 64 (3.2 per cent) teleseismic earthquakes have dynamically triggered seismicity in the SSGF. This indicates that moderate size earthquakes with regional distance within 1000 km from SSGF are more likely to instantaneously trigger seismicity in the SSGF.

To examine possible frequency-dependent threshold for dynamic triggering (Brodsky and Prejean 2005; Peng *et al.* 2009), we compare the amplitude spectra of all the events. The amplitudes of the events that have significant instantaneous dynamic triggering are higher in all frequency ranges, such as the 2010 EMC and the 1999 October 16 M_w 7.1 Hector Mine earthquakes. For other events with instantaneous triggering, the amplitude is generally higher above 0.1 Hz (Fig. 5). This likely follows the threshold function in frequency domain in the Geysers geothermal field: $\varepsilon_T(f) = K/f$, where f is the frequency and K is an empirical value from observations (Gomberg & Davis 1996). However, the 2011 March 11 M_w 9.1, 2010 January 10 M_w 6.5 and 2013 February 06 M_w 8.0 earthquakes did not show systematically higher amplitudes above 0.1 Hz, probably reflecting that other factor might affect the possibility of dynamic triggering, which will be further discussed in Section 5.

We then compare the PGV and the maximum 5 Hz high-pass filtered amplitude of triggered events during surface waves, and find that the PGVs and maximum amplitudes are correlated with a CC value $R = 0.92$ (Fig. 6). Meanwhile, the seismicity rate during surface waves is not well correlated with PGV of the triggering earthquakes (Fig. 6). Our observation is similar to the finding of Aiken *et al.* (2018) that the maximum magnitude of triggered events in the Geysers geothermal field is related to the peak dynamic stress change of main shocks. Here we use maximum amplitude of waveforms after removing the instrument response, instead of event magnitudes, mainly because we do not have the magnitude information of triggered seismicity outside our study period. We note that while the peak amplitude is a consistent estimation of event magnitude, we do not take into account the source–receiver distance. However, since most of the triggered events occurred within the SSGF, the distance factor should not dominate the pattern observed in Fig. 6.

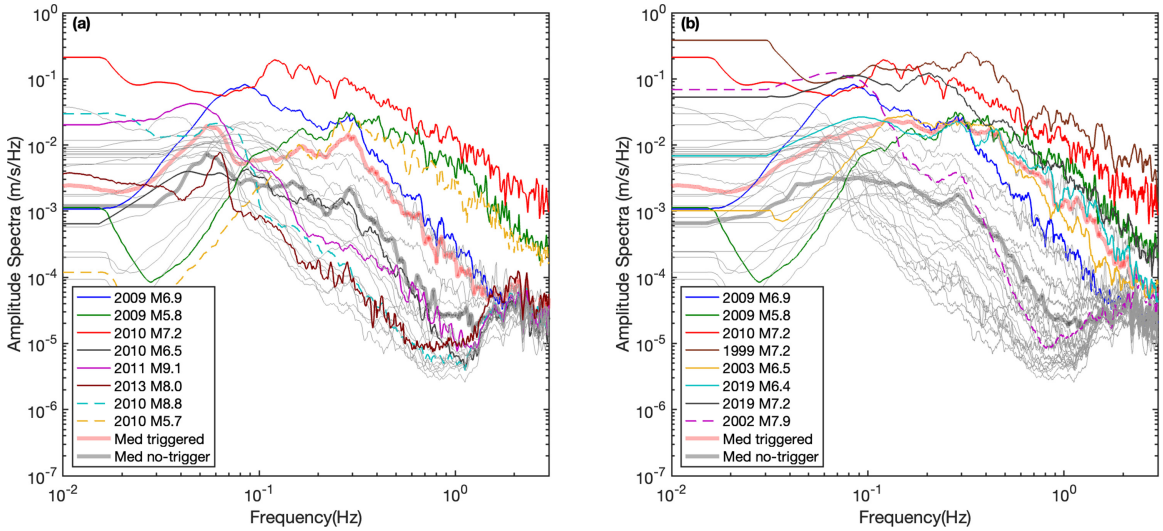

Figure 5. Amplitude spectra of the all the events (a) from 2008 to 2013 and (b) from 1999 to 2019. The earthquakes with positive dynamic triggering are marked with solid, the dashed and grey lines are events with no dynamic triggering. The median spectra of triggering and non-triggering events are marked in the figure.

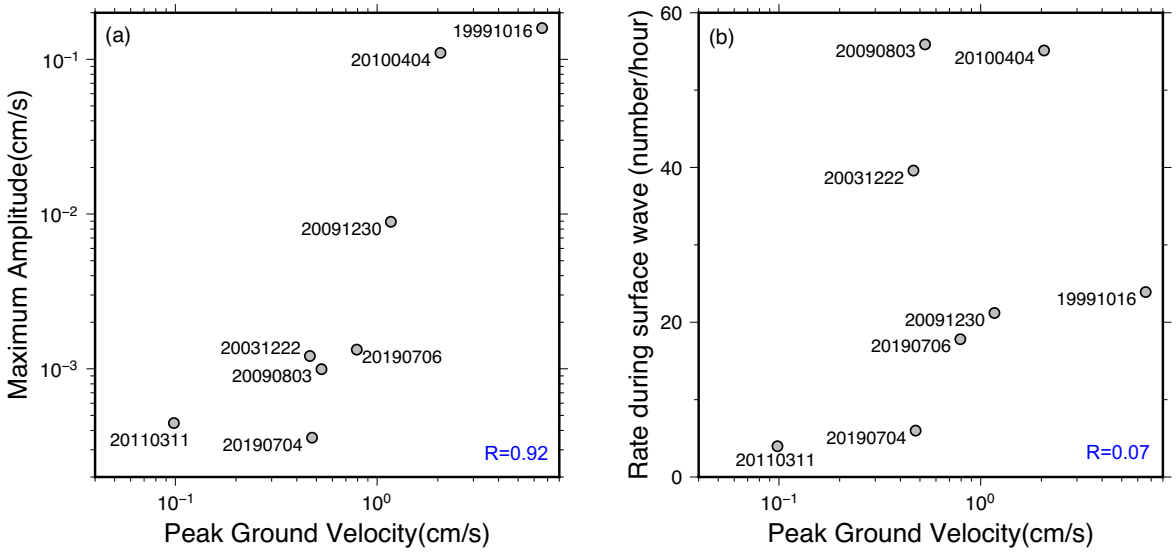

Figure 6. (a) Maximum amplitude of triggered events and (b) seismicity rate during surface wave and versus PGV for all the positive and clear triggering earthquakes.

4 LONG-TERM SPATIAL-TEMPORAL VARIATION OF SEISMICITY

In this section, we evaluate long-term temporal change in seismicity rate and its relationship with distant events and geothermal activities. To further remove the influence of local aftershock triggering effects in the cataloguewe apply a stochastic declustering method based on space–time Epidemic-Type Aftershock Sequence (ETAS) model to the catalogue (Ogata 1988; Zhuang *et al.* 2002, 2004; Zhuang 2006). Detailed steps of the ETAS model are described in the Supplementary Information. Here, we use a 3-month window and cut-off magnitude $Mc = 0$ to make sure that the catalogue is complete, and the algorithm can converge well. Next, we calculate the cumulative background seismicity: $S(t) = \sum_{t<t_i} \varphi_i$, where φ_i is the background probability of the ith event in the catalogue (Meng & Peng 2014). The ETAS parameters are shown in Table S8 (Supporting Information).

4.1 Relationship between seismicity and geothermal activities

Brodsky & Lajoie (2013) analysed the seismicity in the SSGF from 1987 to 2013, and found that the monthly background seismicity rate for events with $M > 1.75$ correlates with the geothermal net production rate and injection rate. In this study, we use our more complete MFD catalogue in 2008–2013 to further analyse potential correlations between geothermal production and seismicity rates. We compare the monthly cumulative background seismicity rate from the ETAS declustered catalogue with the geothermal production/injection and net production rates from 2008 to 2013. Fig. 7(a) shows that there is little correlation between cumulative background seismicity rate for events with $M > 0$ and net production rate or injection and production rates. In comparison, there is a weak correlation between background seismicity with $M > 1.5$ and net production ($R = 0.52$), which is consistent with the

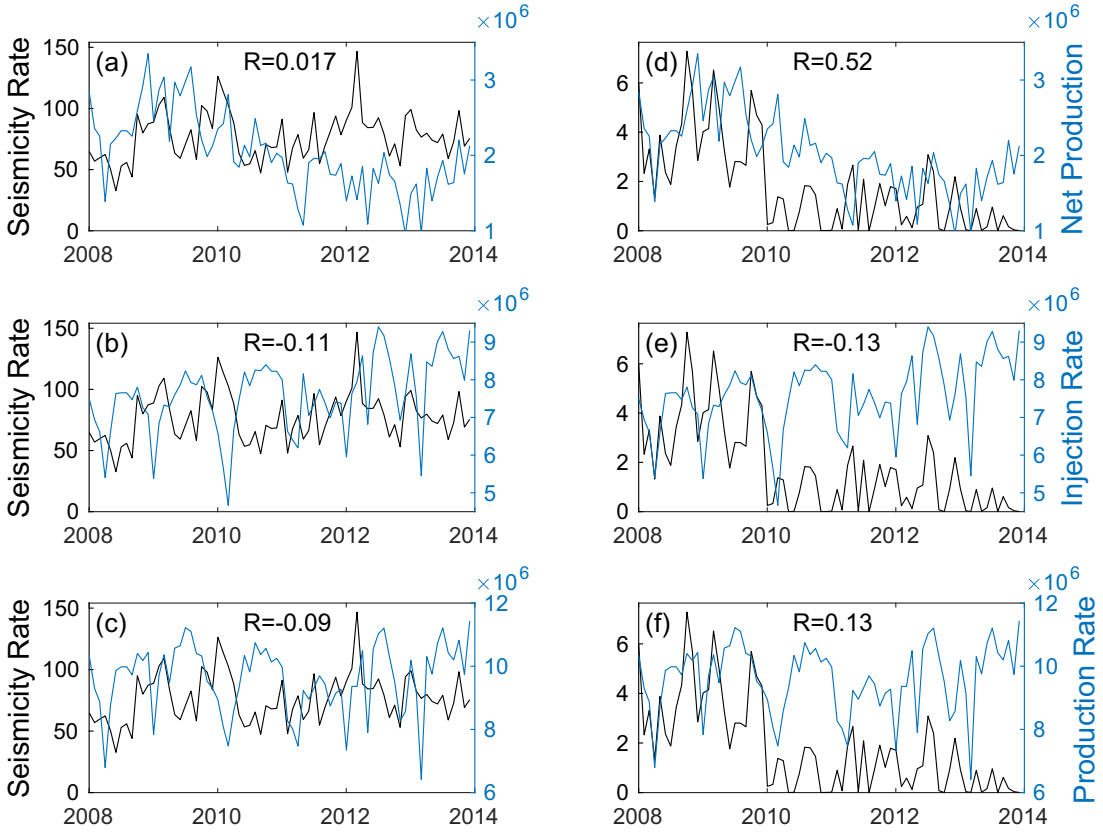

Figure 7. Monthly cumulative background seismicity of events with $M > 0$ in SSGF compared with (a) net production rate (m^3 $month^{-1}$), (b) injection rate and (c) production rate. (d)–(f) Same for events with $M > 1.5$.

pattern found in Brodsky & Lajoie (2013). A subtle increasing trend exists for the background seismicity with $M > 0$. In comparison, for $M > 1.5$ there is a decreasing trend with sudden decrease of seismicity in the beginning of 2010 (Figs 7a and d).

4.2 Spatial and temporal variation of seismicity

With the new MFD catalogue, we examine spatial-temporal evolution of dynamically triggered seismicity in the SSGF. The spatial distribution of seismicity within 1 d since the triggering main shocks are displayed in Fig. S6 (Supporting Information). The local seismicity following the 2010 EMC earthquake appears more widespread in space, while for other three events the triggered earthquakes are more concentrated, and most of them are close to the geothermal injection/production wells. Next, we compare the seismicity increase inside and outside the SSGF. Following Cheng and Chen (2018), events with the nearest lateral distances to injection/production wells of less than 3 km are considered to be inside the geothermal field, and others are considered outside. The seismicity increases inside the SSGF following all the four earthquakes are more abrupt than outside (Fig. 8). Similar pattern is also observed with the QTM catalogue (Fig. S7, Supporting Information), suggesting that the most triggered seismicity, especially right following the distant main shock, are inside the SSGF.

The *b*-value measured from the Gutenberg–Richter frequency–magnitude distribution can be used to investigate the stress state of surrounding regions (Tormann *et al.* 2014; Nishikawa and Ide 2014). Previous studies have found that the *b*-value for events inside the SSGF is higher than events outside the geothermal field (Cheng and Chen 2018). Here we compare *b*-values measured from events inside and outside SSGF for both MFD and SCSN catalogues (Fig. 9). The seismicity inside the SSGF has slightly higher *b*-value than outside for both catalogues. The spatial distribution of *b*-value is shown in Fig. 10(a). The *b*-value of each event with $M > -0.5$ is computed from its 200 nearest neighbours within 3 km in a 3-D distance, and the M_c and *b*-value are estimated with the maximum likelihood methods for at least 50 events above M_c (MAXC + 0.4). Events with high *b*-values are close to the centre of AB cross-section line (with a 45° strike) in the middle of the SSGF, and also close to areas with high density of injection and production wells. The spatial distribution of triggered seismicity in the triggering window T_a of the 6 earthquakes are shown in Fig. 10(b). The regions with higher density of triggered seismicity are likely close to regions with higher *b*-value.

We estimate the temporal change of *b*-value in a 60-d time window and 30-d moving window and require more than 100 events above *Mc* for the time-series of *b*-value inside and outside the SSGF region from 2008 to 2013. The *b*-value time series inside the SSGF are generally higher than those outside the SSGF, indicating there are more small-magnitude events inside the SSGF (Fig. S8, Supporting Information). The time-series of *b*-values inside the SSGF is unrelated to the production rates (Fig. S9, Supporting Information). The *Mc* has a slight negative correlation with the monthly net production rate ($R = -0.33$), indicating an increase of small-magnitude events when the net production rate increases.

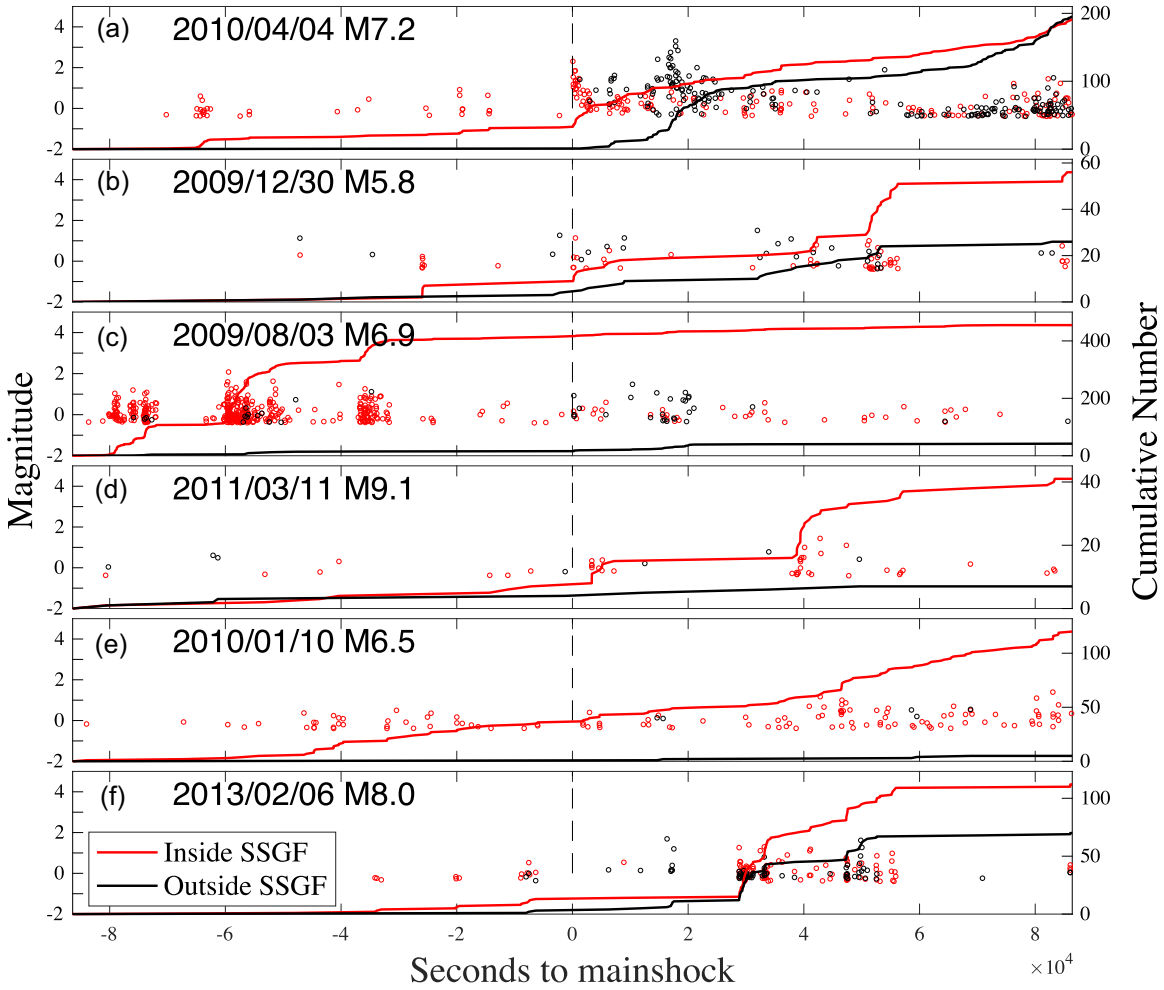

Figure 8. Magnitude and cumulative number of earthquakes in Salton Sea around (a) the 2010 April 04 M_w 7.2, (b) 2009 December 30 M_w 5.8, (c) 2009 August 03 M_w 6.9, (d) 2011 March 11 M_w 9.1, (e) 2010 January 10 M_w 6.5 and (f) 2013 February 06 M_w 8.0 earthquake. The red circles and red lines represent events inside SSGF, while the black circles and lines are events outside SSGF.

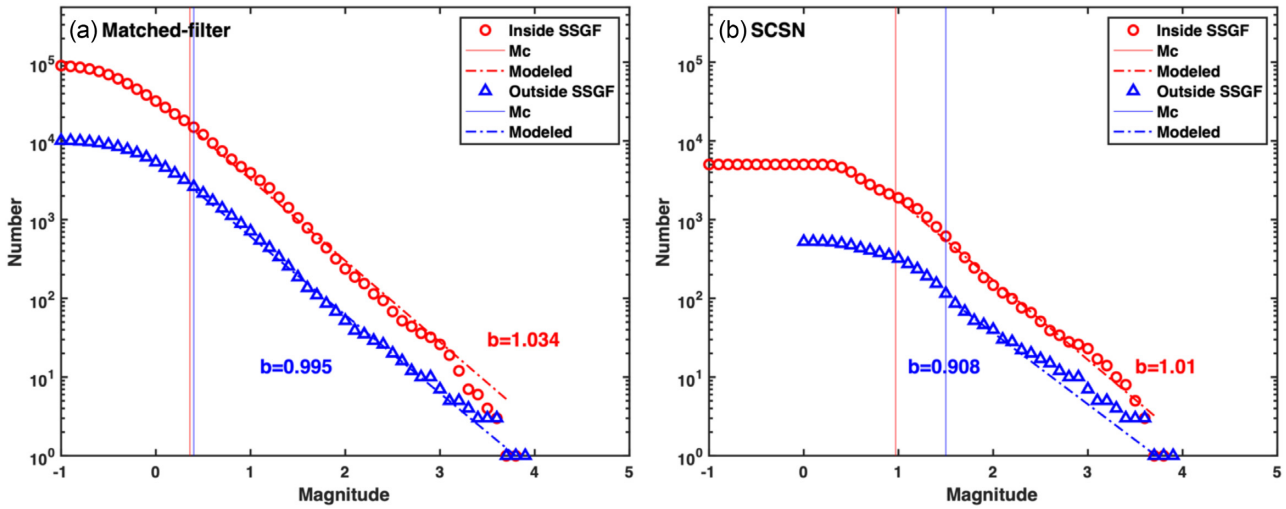

Figure 9. Gutenberg–Richter relationship for events inside and outside SSGF for (a) matched-filter detected (MFD) catalogue and (b) SCSN catalogue from Hauksson *et al.* (2012).

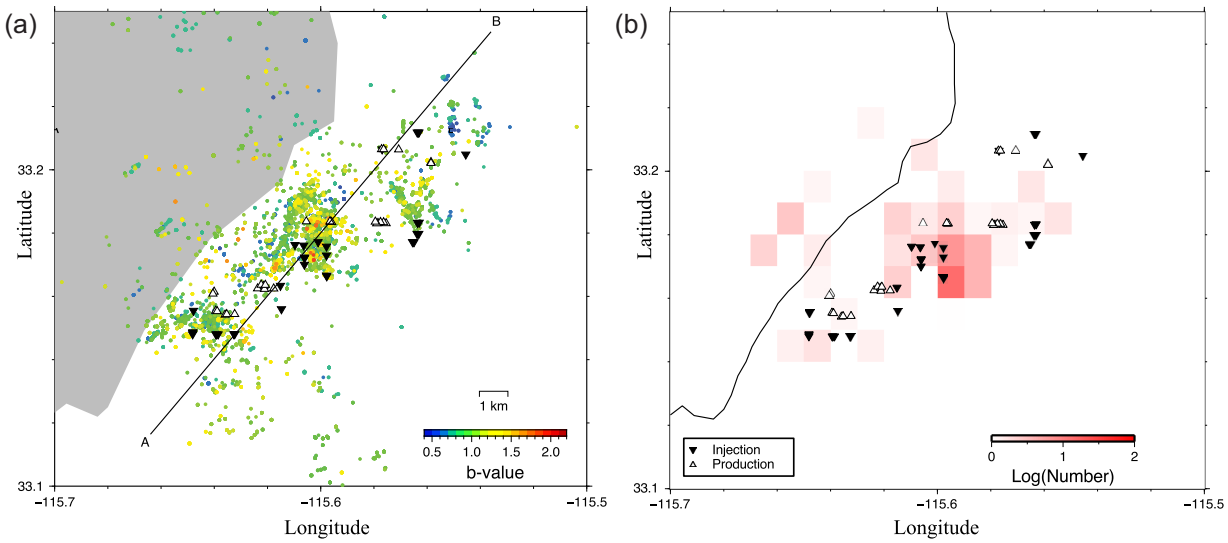

Figure 10. The distribution of *b*-value in (a) map view (b) density of triggered seismicity in in the triggering window T_a of the six triggering earthquakes. The open and invert solid triangles are production and injection wells. respectively.

5 DISCUSSION

In this study, we observe seven *M*5–7.5 earthquakes (three during our MFD catalogue window of 2008–2013, and four outside of this time window) from regional distance and one $M > 9$ teleseismic earthquake (i.e. the 2011 Tohoku-Oki event) that triggered instantaneous seismicity in the SSGF. Previous studies suggest that the amplitude, frequency and azimuth of main shock surface waves are important factors in dynamic triggering (e.g. Brodsky and Prejean 2005; Alfaro-Diaz *et al.* 2020). The regional earthquakes triggered more significant seismicity increase with much larger β statistical value than the only teleseismic earthquake. Many teleseismic earthquakes (such as the 2002 M_w 7.9 Denali and 2010 M_w 8.8 Chile earthquakes) have dynamically triggered microseismicity in other geothermal field in California such as the Coso and Geysers (Prejean *et al.* 2004; Peng *et al.* 2010; Aiken & Peng 2014; Aiken *et al.* 2018). However, these events did not trigger a clear seismicity increase in the SSGF. One reason could be that the surface waves of most regional earthquakes analysed in this study produce high dynamic stress change above 20 kPa, and the SSGF tends to be dynamically triggered at higher dynamic stress. However, the 2002 M_w 7.9 Denali fault earthquake, and an M_w 5.7 event on 2010 June 15 also produced high dynamic stress up to 30 kPa, but they did not appear to have triggered any micro-earthquakes in the SSGF. On the other hand, we find that the peak amplitude of dynamically triggered earthquake correlates with the peak dynamic stress of incoming wave (Fig. 6a). Hence, we argue that the peak amplitude (and peak dynamic stress) is the primary controlling factor for determining the magnitude of the largest triggered earthquake in the SSGF, but is not the only threshold to determine whether the seismicity in SSGF could be dynamically triggered.

Most of the events with significant transient dynamic triggering are regional with distance between 60–1000 km from SSGF, and they have higher amplitude at frequencies above 0.1 Hz (Fig. 5). Compared to the regional earthquakes, the 2002 M_w 7.9 Denali fault earthquake is much weaker at higher frequency ranges. This indicates that the dynamic triggering in SSGF may be frequency dependent. Although some studies suggested that long-period waveforms might be more effective at producing dynamic triggering in volcanic regions, because the fluid flow could act as a low pass-filter (Brodsky and Prejean 2005). There are also evidences that high-frequencies play a role in dynamically triggered seismicity in volcanic and non-geothermal regions (Kane *et al.* 2007; Liu *et al.* 2021). The earthquakes that produce larger high-frequency spectra are generally shallower (depth smaller than 10 km), at regional distance (<1000 km), and their magnitude ranges are between M_w 5.5 to 7.5 However, 2011 M_w 9.1 Tohoku-Oki earthquake generated weak dynamic triggering with relatively small β statistical value, and the other two events that triggered seismicity after 1 d have neither high peak dynamic stress nor high-frequency amplitudes. Thus, there are likely more factors that contribute to dynamically triggered seismicity in the SSGF.

Several studies have suggested that remote earthquakes in the directions aligned with local faults are favourable to dynamic triggering (Chao *et al.* 2012; Aiken et al 2013). Alfaro-Diaz *et al.* (2020) found that distant earthquakes from West Pacific and South America appear to have dynamically triggered more micro-earthquakes in the Coso Geothermal Field than from other regions, and they argued that transient dynamic stresses may align favourably with the local stress field to promote triggering. As shown in Fig. 4(b), the azimuth of the dynamic triggering main shocks are distributed around 90° and 270° from the NE-SW or NNW-SSE strike directions, similar to their study. In addition, the focal mechanisms of local seismicity in the SSGF are mainly dominated by NNW-SSE and NE-SW strike-slip faults (Chen & Shearer 2011). Hence, we cannot argue that incoming incident angles of distant earthquakes play an important role in controlling the triggering behavior here in the SSGF. In addition, the focal mechanisms of 70 per cent (7 out of 10) earthquakes with positive dynamic triggering are strike-slip events (Fig. S10, Supporting Information), which might indicate that the strike-slip events are more likely to trigger seismicity in SSGF. However, another reason could be that regional earthquakes that produce larger energy at higher frequency ranges tend to occur on strike-slip faults.

Previous studies have shown that dynamic triggering is more likely to happen when the local stress states are close to failure (Brodsky and van der Elst, 2014; Hill and Prejean, 2007). We then

investigate whether the *b*-value reveal stress state before the triggered or non-triggered main shocks with the new catalogue. We compute the *b*-value 60 d before the triggering/non-triggering main shocks, and require there are at least 200 events to calculate M_c, and at least 150 events above M_c to calculate *b*-value. The mean *b*-value before triggering and non-triggering main shocks are 0.99 and 0.96, respectively. The Student's test with $p = 0.79$ indicates there is no significant difference in the mean *b*-values at 95 per cent confidence. One possible reason could be that the background stresses are not significantly different before the triggering and non-triggering main shocks. Another possibility that the *b*-values is not sensitive to variations of stress states in the SSGF. Aiken *et al.* (2018) compared the *b*-value of triggered and non-triggered sites in Geysers geothermal field, but the mean value did not show a clear difference. They inferred that the *b*-value may not be a proper 'stress-meter' for the Geysers, consistent with our interpretation. In addition, the SCSN catalogue might be incomplete to detect *b*-value changes, and the uncertainties of event magnitude in the MFD catalogue could also affect the estimation of *b*-values (Herrmann & Marzocchi 2021).

The seismicity in geothermal fields could be affected by other factors, including precipitation, tidal stresses and even shut-down of geothermal productions (i.e. Johnson *et al.* 2017; Cardiff *et al.* 2018; Wang *et al.* 2022). The cumulative monthly rate of $M > 1.5$ events are likely regulated by the monthly net production rate, probably caused by elastic compaction and subsidence due to net volume loss (Brodsky & Lajoie 2013). The slight negative correlation between *Mc* and monthly net production indicates that there is an increase of small-magnitude events when the net production rate increases, and this could be attributed to reduced pore pressures and increases of normal stresses during fluid extractions. Overall, both the dynamically triggered events and long-term seismicity change in the SSGF could be an outcome of interactions among numerous stress disturbances as well as nonlinear pore pressure changes and poro-elastic processes.

6 CONCLUSION

In this paper, we report dynamic triggering cases and examine long-term seismicity change in the SSGF with a more complete MFD catalogue from 2008 to 2013. This study finds that peak dynamic stress and the frequency of incoming seismic waves are the major factors contributing to dynamic triggering in SSGF. The earthquakes with *M*5.5–7.5 from regional distance are more prone to triggering small magnitude events inside the SSGF than other large $M > 8$ events at teleseismic distances. The long-term seismicity shows that $M > 1.5$ events are likely correlated with net geothermal production rates, while smaller events are not regulated by the geothermal production/injection rates. The *b*-values inside SSGF are higher than outside SSGF, and dynamically triggered events are close to locations with high *b*-values. However, temporal change of *b*-values do not predict the potential of triggered seismicity in the SSGF. This study indicates microseismicity with $M < 1.5$ are more sensitive to external stress perturbations from regional earthquakes, and $M > 1.5$ events could be useful to monitor the changes in geothermal operations.

ACKNOWLEDGMENTS

We appreciate SCEDC for making the waveform data and earthquake catalogues open to public. We thank GJI editor Andrew Barbour, assistant editor Louise Alexander, reviewer Ricardo Alfaro-Diaz and one anonymous reviewer for the helpful suggestions to improve this manuscript. This paper benefits from useful discussions with Shengji Wei, Debi Kilb, Emily Brodsky, Wenyuan Fan and Wei Wang. This research was supported by the Southern California Earthquake Center (contribution no. 11964, award nos 10010 and 17230). SCEC is funded by NSF Cooperative Agreement EAR-1600087 and USGS Cooperative Agreement G17AC00047. The GPU-based WMFT utilized the Comet GPU cluster in the XSEDE (eXtreme Science and Engineering Discovery Environment), which is supported by National Science Foundation grant OCI-1053575.

DATA AVAILABILITY

The seismic waveforms in this study are from SCEDC (https://scedc.caltech.edu/index.html). The catalogues for templates and comparison are from alternative catalogues provided on SCEDC website (https://scedc.caltech.edu/eq-catalogs/altcatalogs.html). The monthly geothermal injeciton/production rate is downloaded from the California Department of Conservation website (http://www.conservation.ca.gov/dog/geothermal). The information of all the detected events in the MFD catalogue is in the supplementary catalogue.

REFERENCES

Aiken, C., Meng, X. & Hardebeck, J., 2018. Testing for the 'predictability' of dynamically triggered earthquakes in The Geysers geothermal field, *Earth planet. Sci. Lett.,* **486,** 129–140.

Aiken, C. & Peng, Z., 2014. Dynamic triggering of microearthquakes in three geothermal/volcanic regions of California, *J. geophys. Res.: Solid Earth,* **119**(9), 6992–7009.

Aiken, C., Peng, Z. & Chao, K., 2013. Tremors along the Queen Charlotte Margin triggered by large teleseismic earthquakes, *Geophys. Res. Lett.,* **40**(5), 829–834.

Aki, K. & Richards, P. G., 2002. Quantitative seismology.

Alfaro-Diaz, R., Velasco, A. A., Pankow, K. L. & Kilb, D., 2020. Optimally oriented remote triggering in the Coso geothermal region, *J. geophys. Res.: Solid Earth,* **125**(8), e2019JB019131, doi: 10.1029/2019JB019131.

Aron, A. & Hardebeck, J. L., 2009. Seismicity rate changes along the central California coast due to stress changes from the 2003 M 6.5 San Simeon and 2004 M 6.0 Parkfield earthquakes, *Bull. seism. Soc. Am.,* **99**(4), 2280–2292.

Brodsky, E. E., 2006. Long-range triggered earthquakes that continue after the wave train passes, *Geophys. Res. Lett.,* **33,** L15313, doi:10.1029/2006GL026605.

Brodsky, E. E. & Lajoie, L. J., 2013. Anthropogenic seismicity rates and operational parameters at the Salton Sea Geothermal Field, *Science,* **341**(6145), 543–546.

Brodsky, E. E. & Prejean, S. G., 2005. New constraints on mechanisms of remotely triggered seismicity at Long Valley Caldera, *J. Geophys. Res.,* **110,** B04302, doi:10.1029/2004JB003211.

Brodsky, E. E. & van der Elst, N. J., 2014. The Uses of Dynamic Earthquake Triggering, doi:10.1146/annurev-earth-060313-054648.

Buijze, L. *et al.* 2020. Review of induced seismicity in geothermal systems worldwide and implications for geothermal systems in the Netherlands–CORRIGENDUM, *Neth. J. Geosci.,* **99,** doi: 10.1017/njg.2020.9.

Cardiff, M. *et al.* 2018. Geothermal production and reduced seismicity: correlation and proposed mechanism, *Earth planet. Sci. Lett.,* **482,** 470–477.

Castro, R. R., Clayton, R., Hauksson, E. & Stock, J., 2017. Observations of remotely triggered seismicity in Salton Sea and Coso geothermal regions, Southern California, USA, after big, MW>7.8) teleseismic earthquakes, *Geofis. Int.,* **56**(3), 269–286.

Chao, K., Peng, Z., Wu, C., Tang, C.-C. & Lin, C.-H., 2012. Remote triggering of non-volcanic tremor around Taiwan, *Geophys. J. Int.,* **188**(1), 301–324.

Chen, X., Haffener, J., Goebel, T. H., Meng, X., Peng, Z. & Chang, J. C., 2018. Temporal correlation between seismic moment and injection volume for an induced earthquake sequence in central Oklahoma, *J. geophys. Res.: Solid Earth,* **123**(4), 3047–3064.

Chen, X. & Shearer, P., 2011. Comprehensive analysis of earthquake source spectra and swarms in the Salton Trough, California, *J. geophys. Res.: Solid Earth,* **116**(B9), doi: 10.1029/2011JB008263.

Cheng, Y. & Chen, X., 2018. Characteristics of seismicity inside and outside the Salton Sea geothermal field, *Bull. seism. Soc. Am.,* **108**(4), 1877–1888.

Ellsworth, W. L., Giardini, D., Townend, J., Ge, S. & Shimamoto, T., 2019. Triggering of the Pohang, Korea, earthquake (M w 5.5) by enhanced geothermal system stimulation, *Seismol. Res. Lett.,* **90**(5), 1844–1858.

Fan, W., Barbour, A. J., Cochran, E. S. & Lin, G., 2021. Characteristics of frequent dynamic triggering of microearthquakes in Southern California, *J. geophys. Res.: Solid Earth,* **126**(1), e2020JB020820, doi: 10.1029/2020JB020820.

Fan, W., Okuwaki, R., Barbour, A. J., Huang, Y., Lin, G. & Cochran, E. S., 2022. Fast rupture of the 2009 Mw 6.9 Canal de Ballenas earthquake in the Gulf of California dynamically triggers seismicity in California, *Geophys. J. Int.,* **230**(1), 528–541.

Gibbons, S. J. & Ringdal, F., 2006. The detection of low magnitude seismic events using array-based waveform correlation, *Geophys. J. Int.,* **165**(1), 149–166.

Gomberg, J., Bodin, P., Larson, K. & Dragert, H., 2004. Earthquake nucleation by transient deformations caused by the M = 7.9 Denali, Alaska, earthquake, *Nature,* **427**(6975), 621–624.

Gomberg, J. & Davis, S., 1996. Stress/strain changes and triggered seismicity at The Geysers, California, *J. geophys. Res.: Solid Earth,* **101**(B1), 733–749.

Habermann, R., 1981. Precursory seismicity patterns: stalking the mature seismic gap, *Earthq. Predic.: Int. Rev.,* **4,** 29–42.

Hauksson, E., Yang, W. & Shearer, P. M., 2012. Waveform relocated earthquake catalog for southern California (1981 to June 2011), *Bull. seism. Soc. Am.,* **102**(5), 2239–2244.

Herrmann, M. & Marzocchi, W., 2021. Inconsistencies and lurking pitfalls in the magnitude–frequency distribution of high-resolution earthquake catalogs, *Seismol. Res. Lett.,* **92**(2A), 909–922.

Hill, D. P., *et al.*. 1993. Seismicity Remotely Triggered by the Magnitude 7.3 Landers, California, Earthquake, doi:10.1126/science.260.5114.1617

Hill, D. P. & Prejean, S. G., 2007. Dynamic triggering, *Earthqu. Seismol.,* **4,** 257–291.

Hough, S. E. & Kanamori, H., 2002. Source properties of earthquakes near the Salton Sea triggered by the 16 October 1999 M 7.1 Hector Mine, California, earthquake, *Bull. seism. Soc. Am.,* **92**(4), 1281–1289.

Im, K. & Avouac, J.-P., 2021. On the role of thermal stress and fluid pressure in triggering seismic and aseismic faulting at the Brawley Geothermal Field, California, *Geothermics,* **97,** 102238, doi: 10.1016/j.geothermics.2021.102238.

Johnson, C. W. & Bürgmann, R., 2016. Delayed dynamic triggering: local seismicity leading up to three remote M≥ 6 aftershocks of the 11 April 2012 M8. 6 Indian Ocean earthquake, *J. geophys. Res.: Solid Earth,* **121**(1), 134–151.

Johnson, C. W., Fu, Y. & Bürgmann, R., 2017. Seasonal water storage, stress modulation, and California seismicity, *Science,* **356**(6343), 1161–1164.

Kane, D. L., Kilb, D., Berg, A. S. & Martynov, V. G., 2007. Quantifying the remote triggering capabilities of large earthquakes using data from the ANZA Seismic Network catalog (southern California), *J. geophys. Res.: Solid Earth,* **112**(B11), doi: 10.1029/2006JB004714.

Kim, K.-H., Ree, J.-H., Kim, Y., Kim, S., Kang, S. Y. & Seo, W., 2018. Assessing whether the 2017 M w 5.4 Pohang earthquake in South Korea was an induced event, *Science,* **360**(6392), 1007–1009.

Li, C., Peng, Z., Chaput, J. A., Walter, J. I. & Aster, R. C., 2021. Remote triggering of Icequakes at Mt. Erebus, Antarctica by large teleseismic earthquakes, *Seismol. Soc. Am.,* **92**(5), 2866–2875.

Liu, G. *et al.* 2021. New insights into the 2002-2005 Changbaishan volcanic unrest based on a template matching catalogue, *Front. Earth Sci.,* **8,** 684, doi: 10.3389/feart.2020.599329.

Lohman, R. & McGuire, J., 2007. Earthquake swarms driven by aseismic creep in the Salton Trough, California, *J. geophys. Res.: Solid Earth,* **112**(B4), doi: 10.1029/2006JB004596.

Marsan, D. & Wyss, M., 2011. Seismicity rate changes, *Community Online Resource for Statistical Seismicity Analysis,* doi:10.5078/corssa-25837590.

Martínez-Garzón, P., Kwiatek, G., Bentz, S., Bohnhoff, M. & Dresen, G., 2020. Induced earthquake potential in geothermal reservoirs: insights from The Geysers, California, *Leading Edge,* **39**(12), 873–882.

Matthews, M. V. & Reasenberg, P. A., 1988. Statistical methods for investigating quiescence and other temporal seismicity patterns, *Pure appl. Geophys.,* **126**(2), 357–372.

Meng, X. & Peng, Z., 2014. Seismicity rate changes in the Salton Sea Geothermal Field and the San Jacinto Fault Zone after the 2010 M w 7.2 El Mayor-Cucapah earthquake, *Geophys. J. Int.,* **197**(3), 1750–1762.

Meng, X., Peng, Z. & Hardebeck, J. L., 2013. Seismicity around Parkfield correlates with static shear stress changes following the 2003 Mw6. 5 San Simeon earthquake, *J. geophys. Res.: Solid Earth,* **118**(7), 3576–3591.

Meng, X., Yang, H. & Peng, Z., 2018. Foreshocks, *b* valuemap, and aftershock triggering for the 2011 M_w 5.7 Virginia earthquake, *J. geophys. Res.: Solid Earth,* **123,** 5082–5098.

Meng, X., Yu, X., Peng, Z. & Hong, B., 2012. Detecting earthquakes around Salton Sea following the 2010 Mw7. 2 El Mayor-Cucapah earthquake using GPU parallel computing, *Proc. Comput. Sci.,* **9,** 937–946.

Mignan, A., Landtwing, D., Kästli, P., Mena, B. & Wiemer, S., 2015. Induced seismicity risk analysis of the 2006 Basel, Switzerland, Enhanced Geothermal System project: influence of uncertainties on risk mitigation, *Geothermics,* **53,** 133–146.

Miyazawa, M., Brodsky, E. E. & Guo, H., 2021. Dynamic earthquake triggering in southern California in high resolution: intensity, time decay, and regional variability, *AGU Adv.,* **2**(2), e2020AV000309, doi: 10.1029/2020AV000309.

Nishikawa, T. & Ide, S., 2014. Earthquake size distribution in subduction zones linked to slab buoyancy, *Nature Geosci,* **7,** 904–908, doi:10.1038/ngeo2279.

Ogata, Y., 1988. Statistical models for earthquake occurrences and residual analysis for point processes, *J. Am. Statist. Assoc.,* **83**(401), 9–27.

Pankow, K. L. & Kilb, D., 2020. Going beyond rate changes as the sole indicator for dynamic triggering of earthquakes, *Sci. Rep.,* **10**(1), 1–12.

Panwar, N., Kaushik, S. & Kothari, S., 2011. Role of renewable energy sources in environmental protection: a review, *Renew. Sustain. Energy Rev.,* **15**(3), 1513–1524.

Peng, Z., Hill, D. P., Shelly, D. R. & Aiken, C., 2010. Remotely triggered microearthquakes and tremor in central California following the 2010 M_w 8.8 Chile earthquake, *Geophys. Res. Lett.,* **37,** L24312, doi:10.1029/2010GL045462.

Peng, Z., Vidale, J. E., Wech, A. G. , Nadeau, R. M. & Creager, K. C., 2009. Remote triggering of tremor along the San Andreas Fault in central California, *J. Geophys. Res.,* **114,** B00A06, doi:10.1029/2008JB006049.

Peng, Z. & Zhao, P., 2009. Migration of early aftershocks following the 2004 Parkfield earthquake, *Nat. Geosci.,* **2**(12), 877–881.

Prejean, S. *et al.* 2004. Remotely triggered seismicity on the United States west coast following the M w 7.9 Denali fault earthquake, *Bull. seism. Soc. Am.,* **94**(6B), S348–S359.

Prejean, S. G. & Hill, D. P., 2018. The influence of tectonic environment on dynamic earthquake triggering: a review and case study on Alaskan volcanoes, *Tectonophysics,* **745,** 293–304.

Ross, Z. E., Trugman, D. T., Hauksson, E. & Shearer, P. M., 2019. Searching for hidden earthquakes in Southern California, *Science,* **364**(6442), 767–771.

Shelly, D. R., Ellsworth, W. L. & Hill, D. P., 2016. Fluid-faulting evolution in high definition: connecting fault structure and frequency-magnitude variations during the 2014 Long Valley Caldera, California, earthquake swarm, *J. geophys. Res.: Solid Earth,* **121**(3), 1776–1795.

Shelly, D., Beroza, G. & Ide, S., 2007. Non-volcanic tremor and low-frequency earthquake swarms, *Nature,* **446,**305–307.

Taira, T. a., Nayak, A., Brenguier, F. & Manga, M., 2018. Monitoring reservoir response to earthquakes and fluid extraction, Salton Sea geothermal field, California, *Sci. Adv.,* **4**(1), e1701536, doi: 10.1126/sciadv.1701536.

Tormann, T., Wiemer, S. & Mignan, A. 2014. Systematic survey of high-resolution *b* value imaging along Californian faults: inference on asperities, *J. Geophys. Res. Solid Earth,* **119,** 2029–2054, doi:10.1002/2013JB010867.

Van Der Elst, N. J. & Brodsky, E. E., 2010. Connecting near-field and far-field earthquake triggering to dynamic strain, *J. geophys. Res.: Solid Earth,* **115**(B7), doi: 10.1029/2009JB006681.

Van der Elst, N. J., Savage, H. M., Keranen, K. M. & Abers, G. A., 2013. Enhanced remote earthquake triggering at fluid-injection sites in the mid-western United States, *Science,* **341**(6142), 164–167.

Wang, B., Harrington, R. M., Liu, Y., Yu, H., Carey, A. & van der Elst, N. J., 2015. Isolated cases of remote dynamic triggering in Canada detected using cataloged earthquakes combined with a matched-filter approach, *Geophys. Res. Lett.,* **42**(13), 5187–5196.

Wang, W., Shearer, P. M., Vidale, J. E., Xu, X., Trugman, D. T. & Fialko, Y., 2022. Tidal modulation of seismicity at the Coso geothermal field, *Earth planet. Sci. Lett.,* **579,** 117335, doi: 10.1016/j.epsl.2021.117335.

Woessner, J. & Wiemer, S., 2005. Assessing the quality of earthquake catalogues: estimating the magnitude of completeness and its uncertainty, *Bull. seism. Soc. Am.,* **95**(2), 684–698.

Yao, D., Huang, Y., Peng, Z. & Castro, R. R., 2020. Detailed investigation of the foreshock sequence of the 2010 Mw7. 2 El Mayor-Cucapah earthquake, *J. geophys. Res.: Solid Earth,* **125**(6), e2019JB019076, doi: 10.1029/2019JB019076.

Yao, D., Peng, Z., Kaneko, Y., Fry, B. & Meng, X., 2021. Dynamic triggering of earthquakes in the North Island of New Zealand following the 2016 Mw 7.8 Kaikōura earthquake, *Earth planet. Sci. Lett.,* **557,** 116723.

Yao, D., Peng, Z. & Meng, X., 2015. Remotely triggered earthquakes in South-Central Tibet following the 2004 M W 9.1 Sumatra and 2005 M W 8.6 Nias earthquakes, *Geophys. J. Int.,* **201**(2), 543–551.

Younker, L. W., Kasameyer, P. W. & Tewhey, J. D., 1982. Geological, geophysical, and thermal characteristics of the Salton Sea Geothermal Field, California, *J. Volcanol. Geotherm. Res.,* **12**(3-4), 221–258.

Yun, N., Yang, H. & Zhou, S., 2021. DynTriPy: a python package for detecting dynamic earthquake triggering signals, *Seismol. Res. Lett.,* **92**(1), 543–554.

Yun, N., Zhou, S., Yang, H., Yue, H. & Zhao, L., 2019. Automated detection of dynamic earthquake triggering by the high-frequency power integral ratio, *Geophys. Res. Lett.,* **46**(22), 12977–12985.

Zhang, C., Peng, Z., Liu, X. & Li, C., 2022. *Spatio-Temporal Variations of Shallow Seismic Velocity Changes in Salton Sea Geothermal Field, California,* Earthquake Research Advances.

Zhang, Q., Lin, G., Zhan, Z., Chen, X., Qin, Y. & Wdowinski, S., 2017. Absence of remote earthquake triggering within the Coso and Salton Sea geothermal production fields, *Geophys. Res. Lett.,* **44**(2), 726–733.

Zhuang, J., 2006. Second-order residual analysis of spatiotemporal point processes and applications in model evaluation, *Journal of the Royal Statistical Society: Series B (Statistical Methodology),* **68**(4), 635–653.

Zhuang, J., Chang, C. P., Ogata, Y. & Chen, Y. I., 2005. A study on the background and clustering seismicity in the Taiwan region by using point process models, *J. geophys. Res.: Solid Earth,* **110**(B5), doi: 10.1029/2004JB003157.

Zhuang, J., Ogata, Y. & Vere-Jones, D., 2002. Stochastic declustering of space-time earthquake occurrences, *J. Am. Statist. Assoc.,* **97**(458), 369–380.

Zhuang, J., Ogata, Y. & Vere-Jones, D., 2004. Analyzing earthquake clustering features by using stochastic reconstruction, *J. geophys. Res.: Solid Earth,* **109**(B5), doi: 10.1029/2003JB002879.

SUPPORTING INFORMATION

Supplementary data are available at *GJI* online.

Figure S1. Time-series of SCSN catalogue (templates) and the matched-filter detected earthquakes.

Figure S2. Cumulative number of earthquakes of $M \geq -0.4$ in Salton Sea after six earthquakes in Tables 1 and 2.

Figure S3. Waveform and spectrogram of earthquakes following 2010 April 04 M_w 7.2 EMC earthquake and the 2011 March 11 M_w 9.1 Tohoku-Oki, Japan earthquake.

Figure S4. Waveform and spectrogram of the 2019 July 06 M_w 7.1 Ridgecrest and the 2019 July 04 M_w 6.4 foreshock.

Figure S5. Waveform and spectrogram of the 2003 December 22 M_w 6.5 San Simeon, and 2002 November 03 M_w 7.9 Denali earthquakes.

Figure S6. The triggered events in SSGF after 1 d of the four triggering earthquakes. Red circles are instantaneously triggered events during the passage of surface waves.

Figure S7. Magnitude and cumulative number of earthquakes in Salton Sea from the QTM catalogue one day after (a) the 2010 April 04 M_w 7.2, (b) 2009 December 30 M_w 5.8, (c) 2009 August 03 M_w 6.9 and (d) 2011 March 11 M_w 9.1 earthquake. The red circles and red lines represent events inside SSGF, and the black circles and lines are events outside SSGF.

Figure S8. The *b*-value time series from 2008 to 2013 (a) inside and (b) outside SSGF.

Figure S9. Monthly *b*-value inside SSGF compared with (a) net production rate (m^3 $month^{-1}$), (b) injection rate and (c) production rate. (d)–(f) Same for *Mc*.

Figure S10. PGV versus rake angle λ of all the earthquakes studied from 1999 to 2019. Aki–Richards convention: λ between [−135°,−45°] are strike-slip, λ between [45°,135°] are thrust, and λ within [−45°,45°], [−180°,−135°], [135°,180°] are strike-slip earthquakes, the background of light grey, blue and yellow are normal, thrust and strike-slip event ranges, respectively.

Table S1. Information of all the target earthquakes.

Table S2. Information of the events that have instantaneous dynamic triggering indicated by $\beta \geq \beta_E$, with T_a in surface wave window, $T_b = 60$ da, when the $Mc = 0$.

Table S3. β-, β_E- and Z-values for T_a in surface wave window, $T_b = 60$ d.

Table S4. β-, β_E- and Z-values for T_a in surface wave window, $T_b = 1$ d.

Table S5. β-, β_E- and Z-values for $T_a = 1$ d and $T_b = 60$ d.

Table S6. β-, β_E- and Z-values for $T_a = 1$ and $T_b = 1$ d.

Table S7. Information of $M > 5.5$ earthquakes examined before 2008 and after 2014.

Table S8. Information of ETAS parameters for three-month time windows.

Please note: Oxford University Press is not responsible for the content or functionality of any supporting materials supplied by the authors. Any queries (other than missing material) should be directed to the corresponding author for the paper.